Journal of Nuclear Materials 542 (2020) 152443

Contents lists available at ScienceDirect

Journal of Nuclear Materials

journal homepage: www.elsevier.com/locate/jnucmat

Helium bubble nucleation in Laser Powder Bed Fusion processed 304L stainless steel

Juan Hou[a], Binbin Dai[a], Ying Li[a], Jianguang Zhao[b], Zhuoer Chen[c,d,*], Dong Pan[e], Yuman Zhu[d], Kai Zhang[a,d], Aijun Huang[d]

[a] School of Materials Science and Engineering, University of Shanghai for Science and Technology, Shanghai 200093, China
[b] China Nuclear Power Engineering Co., Ltd., Shenzhen 518124, China
[c] Department of Industrial and Materials Science, Chalmers University of Technology, Gothenburg 41326, Sweden
[d] Monash Centre for Additive Manufacturing (MCAM), Monash University, Notting Hill, VIC 3168, Australia.
[e] Technology Center, Shanxi Taigang Stainless steel Co., Ltd., Taiyuan 030003, China

ARTICLE INFO

Article history:
Received 4 June 2020
Revised 26 July 2020
Accepted 27 July 2020
Available online 8 August 2020

Keywords:
Laser Powder Bed Fusion
Stainless steel
Helium bubble nucleation
Thermal stability
Irradiation tolerance

ABSTRACT

The interest in application of Additive Manufacturing (AM) to nuclear industry stems not only from the benefits of design freedom and shortened lead time, but also from the possibility of enhancing the performance through microstructure control. One of the most important requirements for in-core structural material in nuclear power plants is helium resistance. The Laser Powder Bed Fusion (LPBF) processed 304L stainless steel possesses strong defect sinks such as high densities of dislocation-surrounded sub-grains and dispersed nano-inclusions. In this work the LPBF processed 304L in as-built and solution-annealed conditions along with a conventionally rolled counterpart were implanted with 350 keV He^+ ion at 300 °C to 0.24 dpa (displacement per atom). Transmission Electron Microscopy (TEM) observations indicate significantly higher helium resistance of the as-built LPBF 304L compared to the other two samples. The sink strengths in the three samples are calculated based on the measurements of the microstructural features using simplified equations for the correlation between microstructural characteristics and helium tolerance. Based on the calculation, the cellular sub-grains and the dispersed nano-inclusions are the primary and secondary contributors to the helium resistance of LPBF 304L steel.

1. Introduction

Austenitic stainless steels, as one of the candidate structural materials for nuclear fusion reactors, have the advantages of good mechanical properties, corrosion resistance, and extensive fission operation experience [1,2]. Additive Manufacturing (AM) of stainless steel components is attractive to nuclear industry due to the design freedom it offers and the capability to deliver new component prototypes with complex geometry that is otherwise not achievable in a shorter lead time, thus accelerating the development of new generations of nuclear power plants. It is also desirable for nuclear industry to shorten the supply chain and reduce cost for plant asset management through part consolidation and fast production of high-value components in low volume using AM technologies [3]. Furthermore, it is possible to tailor the microstructure through control of AM processing parameters, which in turn can enhance the material's property and the overall performance of the components [4]. Laser Powder Bed Fusion (LPBF) technology is one of the main metal AM technologies, it melts thin layers of metal powder with a focused laser beam layer by layer to form a three-dimensional part. Compared to other metal AM technologies, LPBF possesses the merits of high resolution, good surface finish and geometrical compliance [5,6].

The rapid solidification, cyclic heating, and spatially variable thermal gradient during the LPBF process introduce a unique microstructure in austenitic stainless steels. Hierarchical microstructures featuring macro-scale columnar grains, ultrafine cellular sub-grains in the majority of studies [7], precipitates [8,9] and oxide nano-inclusions in some studies [10] is obtained.

Irradiation-induced degradation is considered to be one of the main causes for the failure of in-core materials used for nuclear power plants [11]. Various types of defects such as Frenkel pairs and dislocation loops are introduced to the nuclear structural materials due to the continuous collision cascade under neutron ir-

* Corresponding author at: Department of Industrial and Materials Science, Chalmers University of Technology, Gothenburg 41326, Sweden.
E-mail address: zhuoer.chen@chalmers.se (Z. Chen).

https://doi.org/10.1016/j.jnucmat.2020.152443

radiation [12]. Meanwhile, the (n, α) transmutation reaction produces a large number of helium atoms, which are injected into the structural components and aggravate the damage by agglomerating into nanoscale helium bubbles due to their low solubility in metals [12–14]. For laboratory investigations of irradiation damage to materials, the specimen is usually implanted with charged particles (helium ions, heavy ions, protons or electrons) under controlled experimental parameters such as temperature and implantation rate. Specifically, helium ion implantation is widely employed for the study of bubble behaviour. The helium bubbles pose detrimental effects on the mechanical performance of materials such as embrittlement at high temperature [15,16], swelling [17,18] and hardening [19,20].

An effective strategy to enhance the irradiation resistance of materials is to introduce a high density of defect sinks that annihilate point defects during irradiation [21–23]. Examples of such engineered defect sinks are a large number of grain boundaries in nanocrystalline steels [24–26] and particle-matrix interfaces in oxide dispersion strengthened (ODS) steels [27–29]. The sink strengths (efficiency of microstructural features in capturing/annihilating point defects) of grain boundaries and particle-matrix interface in ODS steels have been reviewed in [22] and [23].

The unique microstructural features including ultrafine cellular sub-grains [7,30–33], precipitates [8,9] and oxide nano-inclusion [10,30,33] might benefit irradiation resistance by acting as defect sinks in the LPBF processed austenitic stainless steels. In a study by Sun et al. [34], the equal channel angular pressing (ECAP) process introduced ultrafine grains and high dislocation densities in 304L, which served to delay the onset of high-rate swelling when subject to self-ion irradiation to 60 dpa at 500 °C, while the microstructure shared similarities with LPBF processed 304L. The similarities in microstructure make it interesting to explore the irradiation performance of LPBF 316L and 304L based on the assumptions of the close relationship between microstructure and material's behaviour.

Despite the abundance of literature on the influences of microstructure on bubble behaviour in conventionally manufactured stainless steels [35–37], studies on the irradiation tolerance of LPBF processed austenitic stainless are currently limited in number [38–40]. In this work, we investigate the influence of microstructure on the irradiation resistance of LPBF processed 304L stainless steel in as-built and solution-annealed conditions. Transmission Electron Microscopy (TEM) analysis of samples after implantation of 350 keV He^+ ion at 300 °C showed that the as-built LPBF 304L has the lowest amount of helium bubbles as compared to the solution-annealed LPBF 304L and the conventionally rolled 304L. Analyses of the defect sink strength based on the observations of microstructure are presented to illustrate the important roles played by both cellular sub-grains and dispersed oxide nano-inclusions in enhancing the helium tolerance of LPBF processed material.

2. Experiment

2.1. Sample preparation

The 304L stainless steel studied in this work was manufactured by LPBF machine EOS M280 under argon gas atmosphere using the commercial gas-atomized powder with particle sizes ranging from 10 μm to 53 μm. The LPBF parameters were optimized to achieve a nearly full density with a porosity level below 0.05%. Two LPBF processed 304L samples were prepared for helium implantation, one in as-built condition and the other in solution-annealed condition (1050 °C for 0.5 h, cooling under Ar atmosphere). The third sample was cut out from a 304L plate rolled at room temperature. A final reduction of 50% was reached after eight rolling passes. Table 1 provides the chemical compositions of the as-built LPBF 304L sample and the rolled sample. The three samples of the same size (10 mm × 10 mm × 1 mm) are referred to as the as-built, solution-annealed and rolled samples in the following text for conciseness.

2.2. He^+ ion implantation

The surfaces of the samples were mirror polished and then implanted with 350 KeV helium ions at 300 °C at the Institute of Semiconductors, Chinese Academy of Science. This experimental irradiation temperature (300 °C) was selected using the operation temperature of pressurized water reactor (PWR) as a guide [41]. Resistive heating was applied, the temperature was controlled by adjusting the current passing through a resistance wire. The helium ion irradiation damage profile was estimated using the Stopping and Range of Ions in Matter (SRIM) with the "Kinchin-Pease quick calculation" mode [42]. The helium penetration range was approximately 1 μm in all samples. He^+ ion fluences of 5×10^{16} ions/cm^2 were implanted and generated a peak displacement damage of around 0.24 dpa (displacement per atom) at the location of 0.74 μm below the surface.

2.3. TEM characterization of irradiated samples

Cross-sectional TEM samples were lifted out using a focused ion beam (FIB) technique. To minimize the damage of FIB during sample preparation, the sample was first thinned to around 120 nm under the condition of 30 kV and 21 pA, and further thinned to approximately 50 nm using 2 kV and 17 pA FIB condition. The average foil thickness was further determined to be 45 nm to 53 nm for the LPBF and the rolled samples respectively by convergent beam electron diffraction (CBED) technique (Fig. S1). The number density of helium bubbles in this paper was calculated using a foil thickness of 50 nm for all three samples as an approximation. TEM analysis was conducted using a FEI Tecnai G2F20 microscope operated under 200 kV.

For measurement of bubble density in the samples along the depth direction, a series of TEM images were taken in under-focus and over-focus conditions with some overlapping between one another. Each image for bubble counting covers an area of 145 nm by 145 nm. The depth values for the measured images were taken at the centre of each image.

3. Results

3.1. Helium bubble distribution

Fig. 1 shows the cross-sectional TEM images of the irradiated 304L specimens. No helium bubble is observed near the surfaces of all three samples (Fig. 1(a), (b) and (c)). A noticeable amount of helium bubbles starts to appear in the sub-surface regions at depths of approximately 660 nm, 570 nm and 410 nm in the as-built, solution-annealed and rolled samples, respectively. The helium bubbles appear as bright dots with average diameter below 1 nm in the under-focus and black dots in the over-focus TEM micrographs (Fig. 1). The bubble density increases to its peak maximum at a depth of around 800 nm from the outermost surface for all the three samples. The maximum depths and the widths of bubble damage zone are approximately 1 μm and 340 nm for the as-built sample, 930 nm and 360 nm for the solution-annealed sample, 960 nm and 550 nm for the rolled sample. The depths and widths of the bubble damage zones rank in the order of as-built < solution-annealed < rolled samples.

The number densities of the helium bubbles in the three samples are plotted against the depth from the outermost surface

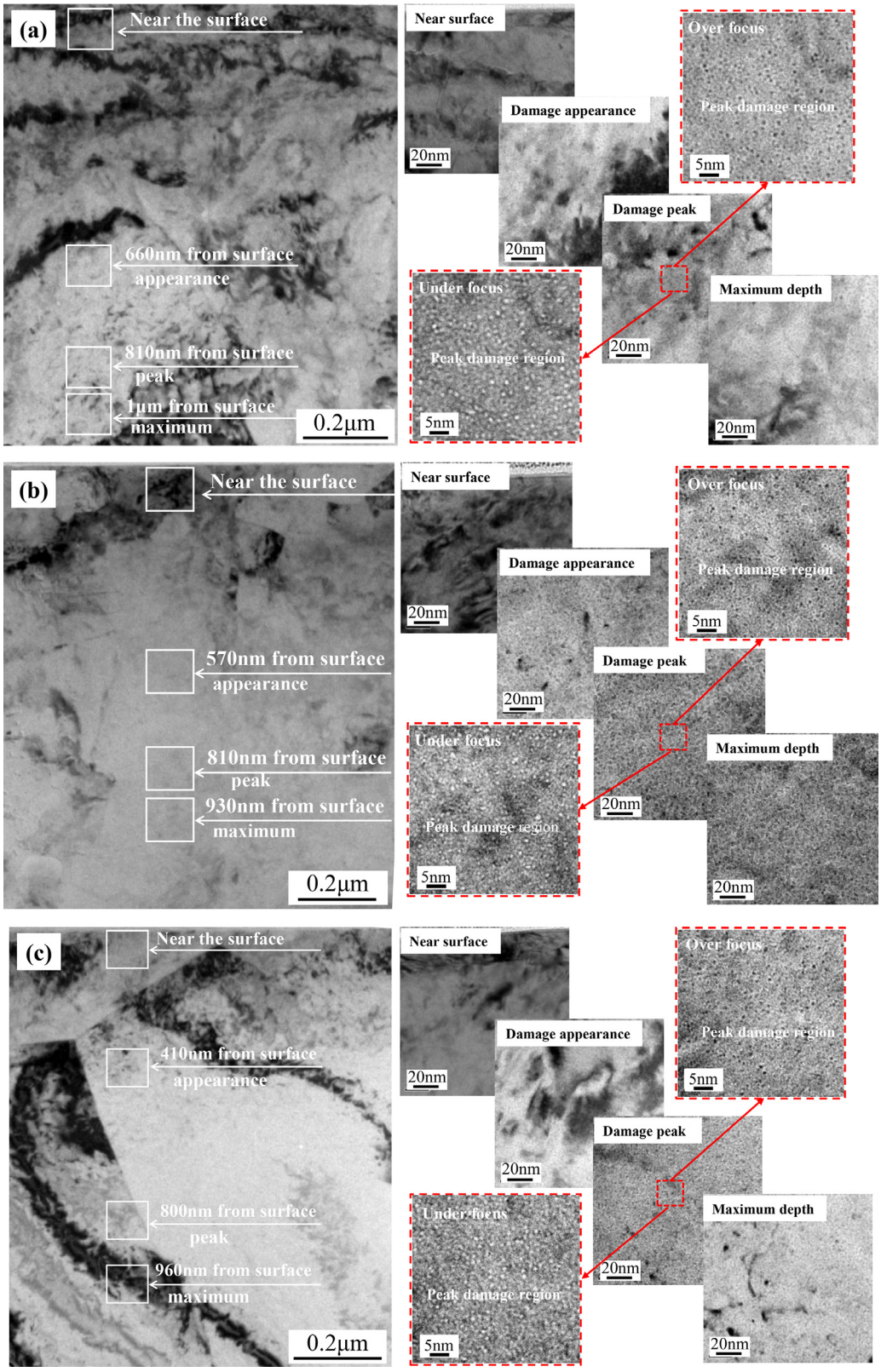

Fig. 1. TEM images taken after helium implantation of (a) the as-built sample, (b) the solution-annealed sample and (c) the rolled sample. For each sample, zoom-in images taken in under-focus and over-focus condition at depth with the peak density of helium bubbles are presented on the right side.

Table 1
Chemical composition of the LPBF 304L and the rolled counterpart (wt. %).

Element	C	N	Si	Mn	P	S	Cr	Ni
As-built	0.014	0.013	0.065	0.054	0.027	0.003	19.07	9.62
Rolled	0.025	0.052	0.471	1.165	0.030	0.002	18.10	8.01

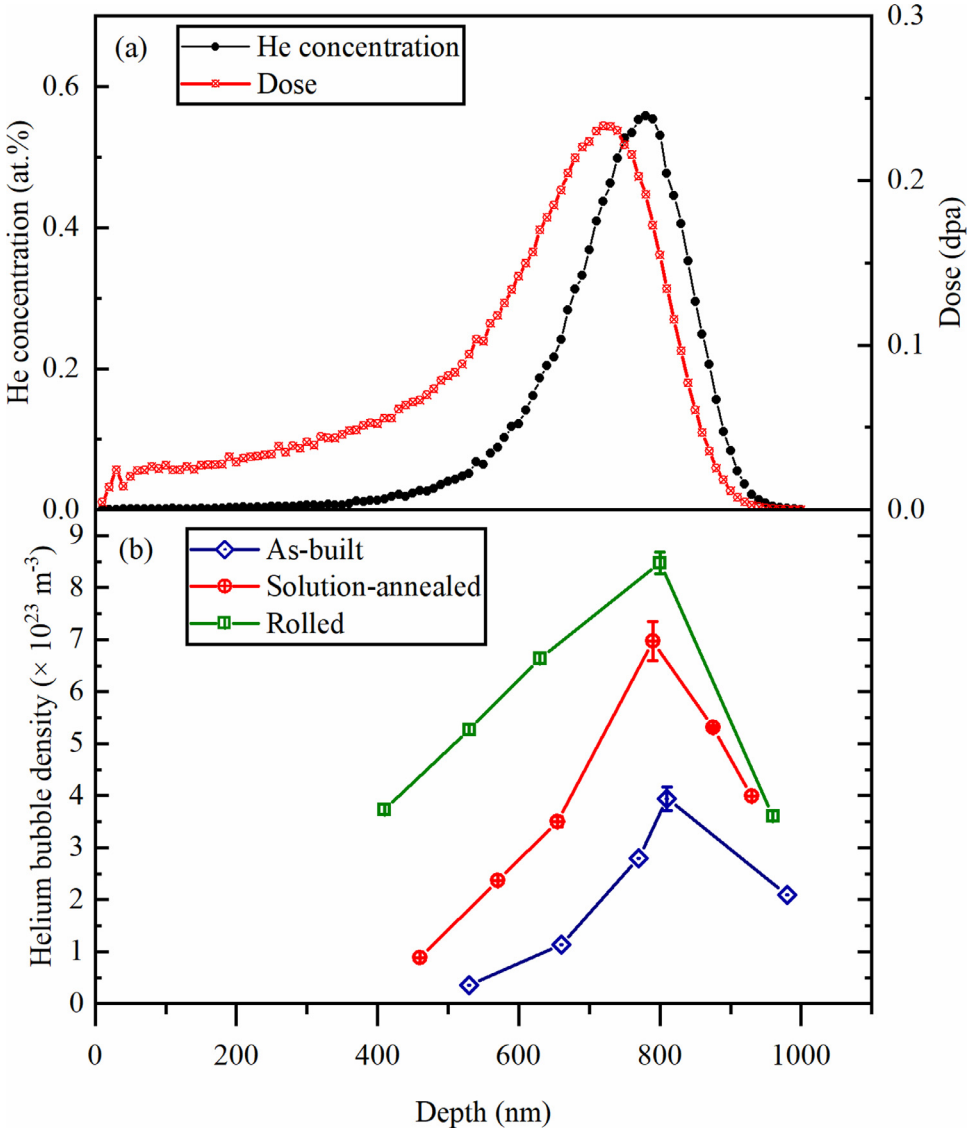

Fig. 2. (a) SRIM calculated damage profile (black line) and He^+ ion implantation profile (red line); (b) measured helium bubble density from TEM images of the as-built, the solution annealed and the rolled samples, error bars are given at peak damage positions based on results of multiple measurements. (For interpretation of the references to colour in this figure legend, the reader is referred to the web version of this article.)

(Fig. 2(b)). The helium bubble density averaged from the depth of bubble appearance to the maximum penetration depth is on the orders of 10^{23} m^{-3}, falling within the range of magnitude from 10^{21} m^{-3} to 10^{25} m^{-3} reported in [13].

The as-built sample has the narrowest bubble damage region and the lowest peak bubble density of around 3.9×10^{23} m^{-3}, as shown by the blue scatters in Fig. 2(b). The damage region of the solution-annealed sample is slightly larger, and the peak bubble density increases to 7.0×10^{23} m^{-3}, as shown by the red scatters in Fig. 2(b). As for the conventionally rolled sample (green scatters in Fig. 2(b)), the resistance to helium bubbles is apparently the lowest, exhibiting the broadest damage region and the highest peak bubble density of 8.5×10^{23} m^{-3}.

3.2. Post-irradiation microstructural characterization

The low dose (0.24 dpa) of the He^+ ion implantation applied in this work is meant to reveal how the nucleation of helium bubbles is influenced by the various microstructural characteristics of the as-built and solution-annealed LPBF 304L as compared to the rolled 304L. Helium bubble nucleation, under the experimental conditions of this paper, is the primary irradiation induced damage phenomenon. There is no significant sign of other types of irradiation-induced defects in the studied samples under TEM, such as dislocation loops.

As shown in Fig. 3(a), the nano-inclusions (marked by the black arrows with dashed lines) are dispersed uniformly throughout the

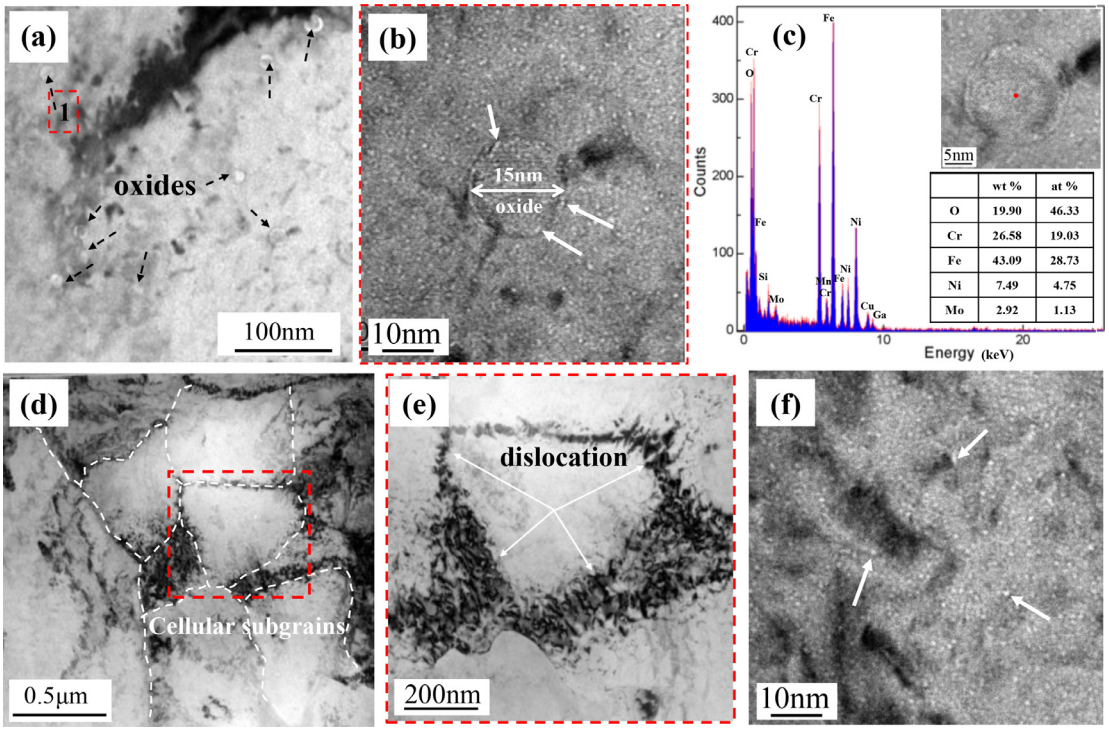

Fig. 3. TEM images showing the helium bubble distribution around defect sinks in the as-built LPBF 304L sample after He^+ implantation: (a) distribution of oxide inclusions in the matrix; (b) magnified view of area 1 in (a) showing an oxide with 15 nm diameter; (c) EDX spectrum at the centre of an oxide inclusion indicated by red spot; (d) cellular sub-grains decorated by dislocation network; (e) magnified view of a cellular sub-grain; (f) distribution of helium bubbles around dislocations. In (b), (c) and (f) the white arrows point to slightly larger helium bubbles in the vicinity of oxide-matrix interface and dislocations. (For interpretation of the references to colour in this figure legend, the reader is referred to the web version of this article.)

matrix of an as-built sample with diameters between 10 nm and 20 nm and a number density of approximately 2.0×10^{20} m^{-3}. A higher magnification image in Fig. 3(b) shows that the interfaces between the nano-inclusion and its surrounding matrix act as defect sinks. Helium bubbles with larger size tend to appear at the inclusion-matrix interfaces (marked as the white arrows), whereas only a few could be found in the areas close to the interface and on the oxide island. The nano-inclusions are identified as Cr-rich oxides by EDX (Energy-dispersive X-ray spectroscopy) point analysis under TEM (Fig. 3(c)). The volume fraction of nano-inclusions determined by image analysis in the as-built sample is approximately 0.19 vol.%. These Cr-rich oxides in the as-built sample are significantly smaller in both size and volume fraction compared the Si- and Mn-rich oxides reported in [10,39] for the LPBF 316L showing an average size of 50 to 60 nm and an amount of about 5 vol.%. Another different case is found in LPBF processed 316L [43] where the Si- and Mn-rich oxide inclusions are approximately 300 nm in size and constitute a 0.23 vol.%. Nano-sized features of similar size have been reported in [44] for LPBF processed 304L, while the features are again rich in Si and Mn, different from what is found in the current study. Possible reasons for this difference might be the higher Cr amount in 304L alloy composition compared to 316L and the particularly low content of Mn (0.016 wt.%) and Si (0.065 wt.%) in the 304L feedstock powder as compared to the previously reported 316L [10,39,43] and 304L [44] powders.

Cellular sub-grains with size less than 500 nm are found in the as-built LPBF 304L sample (Fig. 3(d)). The bright-field image at higher magnification (Fig. 3(e)) shows that the cellular sub-grain boundaries are decorated with high-density entangled dislocations. According to Fig. 3(f), the helium bubbles decrease in number but increase in size in areas surrounding the dislocations (marked as the white arrow) while no helium bubbles could be identified inside the dislocations.

Table 2
Chemical composition of the oxide nano-inclusions measured by TEM-EDS.

		O	Cr	Fe	Ni	Mo
As-built	wt%	19.90	26.58	43.09	7.49	2.92
	at%	46.33	19.03	28.73	4.75	1.13
Solution-annealed	wt%	48.47	49.46	1.87	0.18	0.00
	at%	75.40	23.67	0.83	0.08	0.00

The cellular sub-grains and the dislocation walls disappeared after the solution-annealing treatment, as shown in Fig. 4(a). The oxide nano-inclusions coarsened and changed from spherical shape to faceted ones, while the oxygen and chromium contents significantly increased (Fig. 4(b), Table 2). The coarsening of the nano-inclusions (from 10–20 nm to around 80 nm) is accompanied by the decrease in number density to approximately 2.5×10^{19} m^{-3}. Both microstructural changes lead to the loss of sink strength in the solution-annealed samples. Consequently, the helium bubbles are higher in number (Fig. 2(b)) and more homogeneous in the distribution in the solution-annealed sample (Fig. 4(c)).

In the rolled sample, the helium bubbles show a relatively even distribution (Fig. 5(c)) due to the absence of prevalent defect sinks found in the as-built and solution-annealed samples. The well-known sinking effect of grain boundaries [45] in the rolled sample is expected but not characterized in detail since it is not the focus of the current work.

4. Discussion

4.1. Analysis of sink strength

The present work evaluates the helium resistance of LPBF 304L samples in the as-built condition where cellular sub-grains and

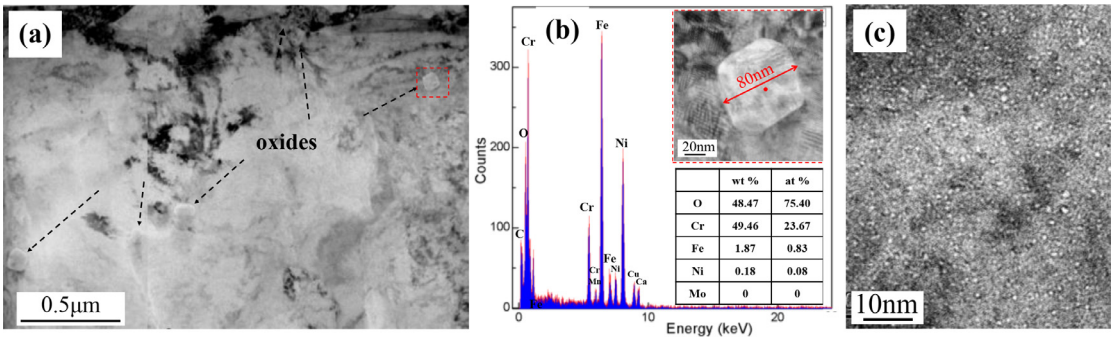

Fig. 4. TEM images of the solution annealed LPBF 304L sample after He^+ implantation. (a) distribution of oxide inclusions in the matrix; (b) EDX spectrum at the centre of an oxide particle with a diameter of 80 nm; (c) helium bubble distribution at higher magnification.

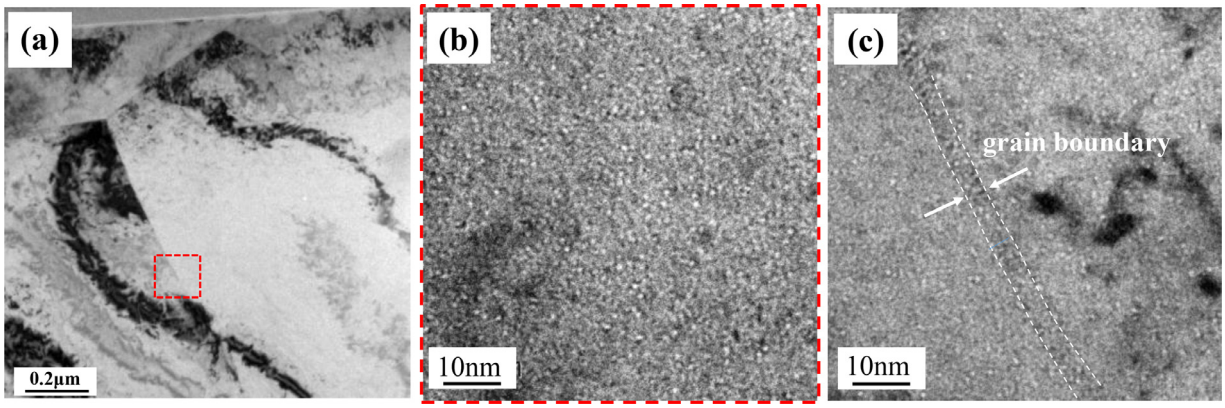

Fig. 5. TEM images of the rolled 304L sample after He^+ implantation. (a) an overview microstructure; (b) distribution of helium bubbles in the area enclosed by red square in (a); (c) helium bubbles appear aligned at a grain boundary, corresponding to the area marked by red square in (a). (For interpretation of the references to colour in this figure legend, the reader is referred to the web version of this article.)

nano-inclusions both act as defect sinks and in solution-annealed condition where nano-inclusions remain as defect sinks. The temperature of He^+ ion implantation implemented in this paper, i.e. 300 °C, falls in the low temperature regime ($T < 0.5\ T_m$). In this regime, the homogenous bubble nucleation at helium traps (helium bubble nuclei, vacancies) in the lattice matrix and the heterogeneous bubble nucleation at defects intrinsic to the material or introduced by irradiation damage are two competitive mechanisms [13]. According to our TEM observation of the He^+ ion implanted, as-built sample (Fig. 3), the heterogeneous bubble nucleation is the dominant one in the vicinity of the defects, where the sink strength of the defects existing in the material (sub-grain boundaries and nano-inclusions) overpowers the sink strength of helium traps in the matrix. Considering the low dose of He^+ ion implantation, the bubble nucleation in the current study is in its initial stage, where small bubbles only start to appear without significant growth. As Shang et al. [38] suggested the dislocations at the boundaries of cellular sub-grains are neutral defect sinks, due to the overlap of capture radii of the dislocations and partial cancellation of long-range stress field among the entangled dislocations. Therefore, the dislocations at cellular sub-grain boundaries can capture both interstitials and vacancies with almost equal efficiency and allow them to cancel out. The ample and effective defect sinks in the as-built sample immobilize helium atoms and at the same time trap and annihilate point defects, preventing the formation of helium bubble nuclei such as helium-vacancy clusters. For the solution-annealed sample and the rolled sample with less defect sinks, the bubbles nucleate at locations farther away from peak damage depth predicted by SRIM where the injected helium is of less amount, as shown in Fig. 2. Consequently, the helium damage zone appears the narrowest for the as-built sample with the highest sink strength and widest for the rolled sample with less defect sinks.

Fig. 6 illustrates schematically the presence of defect sinks in the three 304L materials investigated, the sink strength decreases following the order of the as-built, solution annealed and rolled samples while the helium bubble damage zone widens and the peak bubble density increases. Here we calculate with approximations the sink strengths in the three 304L samples. The sink strengths of grain boundaries, k^2_{gb}, can be calculated using formula (1) derived using cellular model when the internal sink strength is very small compared to the sink stregnth of grain boundaries [46].

$$k^2_{gb} = {}^{15}/_{R^2} \tag{1}$$

where R is the radius of the (sub-)grains. Assuming equivalent sinking efficiencies by cellular walls and high angle grain boundaries (HAGBs), while using (sub-)grain radius values of 0.25 μm, 10 μm and 20 μm for the as-built, solution-annealed and rolled samples, the sink strength provided by (sub-)grain boundaries are calculated as $2.4 \times 10^{14}\ m^{-2}$, $6 \times 10^{11}\ m^{-2}$, and $1.5 \times 10^{11}\ m^{-2}$, respectively. This is not a very rigorous calculation, since the cellular sub-grain boundaries are decorated by dislocations and show little to none misorientations. One might choose to calculate the sink strength of cellular walls using the formula for the sink strength of dislocations instead, i.e. formula (2) [47]

$$k^2_d = \rho_d Z_d \tag{2}$$

where k^2_d denotes the sink strength of dislocations, ρ_d is the dislocation density and Z_d is the sink capture efficiency of dislocations. However, the dislocations in the as-built material aggregates at sub-grain boundaries, performing a sinking effect as boundaries

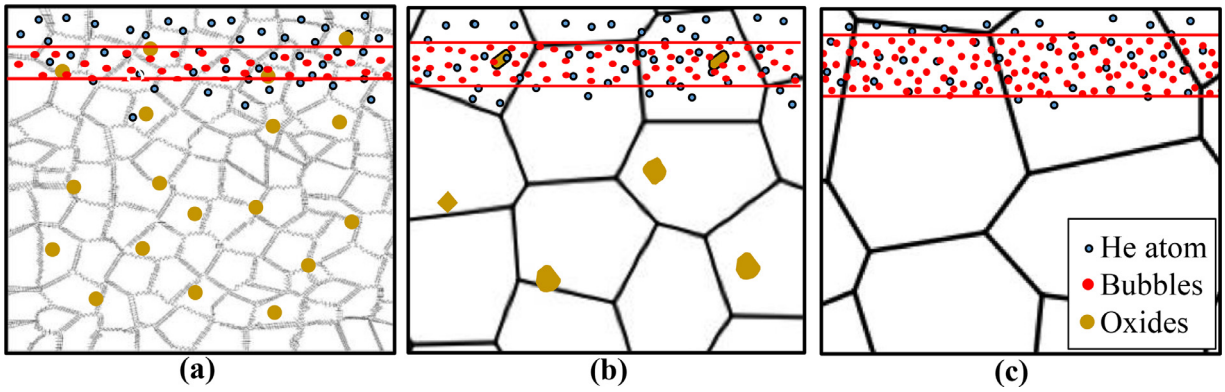

Fig. 6. Schematics to illustrate the effect of microstructure on helium bubble nucleation in the compared three samples: (a) the as-built sample, (b) the solution-annealed sample and (c) the rolled sample. (For interpretation of the references to colour in this figure legend, the reader is referred to the web version of this article.)

rather than diffused dislocation networks, it is therefore reasonable to calculate the sink strength of cellular sub-grain boundaries using formula (1). A similar approach was adopted by Song et al. [40].

The sink strengths of nano-inclusions in the as-built and solution-annealed samples, k_c^2, can be calculated using formula (3), which was initially derived in [48] to calculate the sink strength of cavities, but can be used for calculating the sink strength of dispersoids or precipitates as well [23].

$$k_c^2 = 4\pi r_c N_c (1 + k r_c) Z_c \quad (3)$$

where r_c is the radius of inclusion, N_c is the number density of nano-inclusions, k is the square root of the cumulative sink strength of all sink types, k^2, and Z_c is the sink capture efficiency of order unity [23]. For approximate calculation, we take $Z_c = 1$. We also assume that point defects and dislocations are mostly consumed by (sub-)grain boundaries due to their strong sinking effects, therefore the cumulative sink strength can be approximated by the sink strength of (sub-)grain boundaries, so that $k^2 \approx k_{gb}^2$. The measured average radius and number densities of nano-inclusions are 7.5 nm and 2.0×10^{20} m^{-3} for as-built condition, 40 nm and 2.5×10^{19} m^{-3} for solution-annealed condition. The calculated sink strengths provided by nano-inclusions for the as-built and solution-annealed LPBF 304L are 2.1×10^{13} m^{-2} and 1.3×10^{13} m^{-2}, respectively. We can infer from the above calculation that the change in nano-inclusions from as-built to solution-annealed state in terms of size and number density accounts for a moderate contribution to the difference between as-built and solution-annealed LPBF samples, while the loss of cellular sub-grains as defect sinks has more dominant effect. This comparison provides a rough estimation of the extent to which the sink strength decays with prolonged exposure to elevated temperature and irradiation damage due to the instability of cellular sub-grain structure. As one sums up the sink strengths provided by (sub-)grain boundaries and nano-inclusions, the cumulative sink strengths are 2.6×10^{14} m^{-2}, 1.4×10^{13} m^{-2} and 1.5×10^{11} m^{-2} for the as-built, solution-annealed and rolled 304L respectively, as summarized in Fig. 7. The solution-annealed LPBF 304L has a sink strength that is about one order of magnitude less than the as-built one but is two orders of magnitude greater than the conventionally rolled 304L.

It should be clarified that the sink strength of the rolled sample is more complex and therefore the comparison is not as straightforward as the current presentation. Taking into account the shallow implantation of He^+ ions in the current study (~ 1 μm) the grain size effects make little contribution to the difference observed between the solution-annealed sample and the rolled sample despite the difference in calculated sink strength of (sub-)grain boundaries. In addition, the cold rolling process can introduce deformation-induced martensitic phase transformation and evolution of dislocations [49,50], which would affect the sink strength of the rolled sample. X-ray diffraction results showed that all three samples in the current study are fully austenitic (Fig. S2). According to the TEM characterization of dislocations of unirradiated samples (Fig. S3), the rolled sample possessed a moderate density of dislocations, much lower than the as-built LPBF sample. Therefore the effect of dislocations on the sink strength of rolled sample was neglected for simplicity of the analysis.

4.2. Enhanced irradiation tolerance in LPBF steel

A major proportion of the sink strength in LPBF processed stainless steel comes from the cellular sub-grains with average diameters ranging from 380 nm to 500 nm [38–40,44]. As a comparison, the HAGBs achieved by severe plastic deformation, such as high pressure torsion (HPT) [24–26] and ECAP [51], exhibit smaller average size (usually under 100 nm). According to the inverse relationship between k_{gb}^2 and grain size, sink strength of (sub-)grain boundaries in LPBF processed austenitic stainless steel is weaker compared to the nanocrystalline counterparts reported in [24–26,51]. However, direct comparison is needed for firm conclusion since the defect capture efficiency must be different for HAGBs and cellular dislocation walls.

The effectiveness of defect sinks lies in the sink strength, the sink capture efficiency, the bias towards different types of defects (interstitials, vacancies) and how the sink strength holds over long-term exposure to elevated temperature and irradiation. In the experiment of Shang et al. [38], the dislocation walls at the sub-grain boundaries became wide and diffuse but remained stable and effective defect sinks for irradiation induced dislocation loops during Kr^{++} heavy ion implantation at 400°C to 5 dpa. Similarly, the cellular sub-grains in LPBF processed 316L did not change in size and morphology after He implantation at 450 °C to approximately 0.8% He concentration in the work of Sun et al. [39], where excellent helium tolerance was found. In contrast, there are cases where the cellular sub-grains in LPBF processed 316L and 304L lacked stability, or even proved detrimental to irradiation tolerance. Song et al. [40] compared LPBF 316L samples in stress relieved (SR) and hot isostatic pressing (HIP) condition after proton irradiation at 360 °C to 2.5 dpa. The cellular sub-grains in the SR sample showed recovery and recrystallization due to the irradiation-enhanced diffusivity and more severe swelling compared to HIP sample due to its intermediate dislocation density [40]. It is worth mentioning that in [40] the SR treatment at 650 °C (within sensitization temperature range of 316L) might alter the microstructure while the samples in the former two studies [38,39] were in as-built condition.

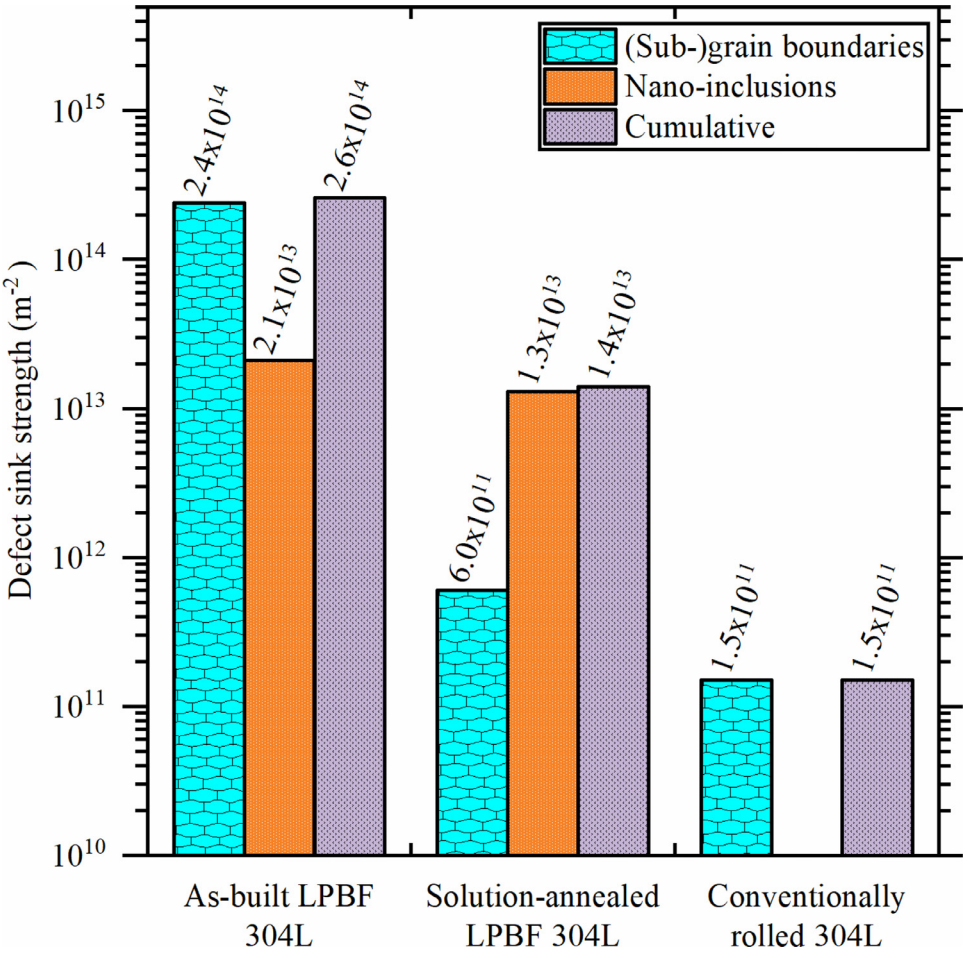

Fig. 7. Effects of grain size and oxide inclusions on the sink strengths in the as-built LPBF, the solution annealed LPBF, and the rolled 304L stainless steel.

In addition, Eftink et al. [44] also observed instability of the cellular sub-grains in LPBF processed 304L after proton irradiation at temperatures below 300 °C up to 12 dpa and explained the instability with irradiation-enhanced diffusion as well.

Meanwhile, the finely distributed nano-inclusions in the LPBF 304L (both as-built and solution-annealed) presents a new potential way of making ODS steels, which was also pointed out by Zhong et al. [30]. The introduction of many cavity defect sinks into the material leads to the nucleation of a high number density of helium bubbles and thereby providing sites for annihilation of opposite types of point defects and at the same time delaying bubble growth [23]. The number density of nano-inclusions achieved unintentionally by the current study is far below the necessary level ($> 5 \times 10^{23}$ m^{-3}, leading to a cavity sink strength of larger than 10^{16} m^{-2}) for the material to be considered as of superior radiation resistance [23,52]. However, there is a possibility to further increase the concentration of nano-inclusions, either by manipulation of feedstock powder composition or atmosphere of the processing chamber [30].

Although the thermal stability of defect sinks was not thoroughly studied, the respective contributions of two types of defect sinks in cellular sub-grains and nano-inclusions and their cumulative effects on helium bubbles tolerance are discussed in this work. The co-presence of two types of defect sinks makes the LPBF 304L an attractive material for nuclear applications. The sink strength of LPBF 304L analyzed in this paper is not up to the standard of superior radiation-resistant materials, but still better than a conventionally rolled sample. This is not to mention that LPBF as an AM process allows more geometrical freedom and complexity of the part compared to powder metallurgy or deformation processes.

4.3. Limitation of the current work

Although the chemical composition was not a controlled factor in the present study, it is necessary to acknowledge its possible influence on helium bubble nucleation. As shown in Table 1, the LPBF processed 304L sample has slightly higher content in both Ni and Cr, and lower contents in minor elements, most noticeably in Si, compared to the rolled 304L sample. According to [53], main alloying elements, primarily Fe, Ni and Cr, affects the effective vacancy diffusion coefficient and thereby change the accumulation behaviour of vacancy and available sites for bubble nucleation, i.e., slower vacancy diffusion leads to a higher likelihood of forming He-vacancy clusters. The addition of minor elements such as P and Si has nonmonotonic effects due to the two competing effects: (1) solute-interstitial binding at lower content; (2) enhanced vacancy diffusion at higher content. Since the two compositions deviate in the contents of many elements and the influences of the elements are synergistic, a direct comparison between the rolled sample and the LPBF processed samples (as-built and solution-annealed) in terms of irradiation resistance is not possible. Instead, the rolled 304L sample is used as a parallel experiment for revealing differences between a conventionally manufactured 304L (cold-rolled) and a LPBF processed 304L in terms of helium bubble nucleation behaviour through detailed microstructure characterization. Furthermore, due to the shallow implantation of the current study (less than 1 μm) as compared to the grain size

(several tens of micrometres), the sink strength provided by the grain boundaries did not play a prominent role in the current paper. The analysis and discussion of the sink strength in the preceding sections (4.1 and 4.2) are for demonstration of how the irradiation tolerance can be enhanced by the LPBF process and the potential for further improvement rather than for comparison.

Based on the limitation of the current work, further investigations are recommended as follows for understanding the irradiation resistance of LPBF austenitic steels:

1) controlled experiments in the chemical composition of LPBF powder feedstock with differing contents of important minor elements (e.g. P and Si) and their impacts on irradiation tolerance;
2) comparison between severely deformed (e.g., HPT and ECAP) and LPBF processed samples to study the differences between HAGBs and cellular sub-grains in defect capture efficiency;
3) varied helium implantation conditions (temperature, helium fluence, implantation dose) for more comprehensive evaluations of helium damages in LPBF processed samples.

5. Conclusions

The helium bubble nucleation in LPBF processed 304L alloy in as-built and solution-annealed state was analyzed using TEM after 350 KeV He^+ implantation at 300 °C to 0.24 dpa with contrast to a conventionally rolled counterpart. The LPBF processed 304L samples, in as-built and solution-annealed condition, exhibit better tolerance to helium bubble formation, which is manifested by narrower helium damage zones and lower number densities of bubbles. The unique microstructure of LPBF 304L in as-built condition contains strong defect sinks in sub-grain boundaries decorated with dislocation walls and the interfaces between dispersed nano-inclusions and the matrix. After solution-annealing, the merging of the sub-grains and the coarsening of nano-inclusions reduce the helium tolerance. Approximate calculations of the sink strengths suggest that the sub-grain boundaries suppress helium bubble nucleation to a larger extent compared to the dispersed nano-inclusions in the studied LPBF 304L material. Although depleted of sub-grain boundaries, the solution-annealed sample exhibits a moderate helium resistance with thermally stable microstructure.

Declaration of Competing Interest

The authors declare that they have no known competing financial interests or personal relationships that could have appeared to influence the work reported in this paper.

CRediT authorship contribution statement

Juan Hou: Conceptualization, Methodology, Investigation, Writing - original draft, Writing - review & editing. **Binbin Dai:** Investigation. **Ying Li:** Investigation. **Jianguang Zhao:** Funding acquisition. **Zhuoer Chen:** Conceptualization, Methodology, Formal analysis, Writing - original draft, Writing - review & editing. **Dong Pan:** Resources, Writing - review & editing. **Yuman Zhu:** Writing - review & editing. **Kai Zhang:** Investigation, Writing - review & editing. **Aijun Huang:** Funding acquisition, Supervision, Project administration.

Acknowledgements

This research was sponsored by the Special funds for Future Industries of Shenzhen (Project No. JSGG20170824104916638) and the National Key R&D Program of China (Grant No. 2018YFB1106100). Great thanks to Dr. Li Jianjian for the helpful discussion.

Supplementary materials

Supplementary material associated with this article can be found, in the online version, at doi:10.1016/j.jnucmat.2020.152443.

References

[1] S. Şahin, M. Übeyli, A review on the potential use of austenitic stainless steels in nuclear fusion reactors, J. Fusion Energy 27 (2008) 271–277, doi:10.1007/s10894-008-9136-3.
[2] R. Baldev, U.K. Kamachi Mudali, M. Vijayalakshmi, M.D. Mathew, A.K. Bhaduri, P. Chellapandi, S. Venugopal, C.S. Sundar, B.P.C. Rao, B. Venkataraman, Development of stainless steels in nuclear industry: With emphasis on sodium cooled fast spectrum reactors: History, technology and foresight, Adv. Mater. Res. 794 (2013) 3–25 10.4028/www.scientific.net/AMR.794.3.
[3] R.B. Rebak, X. Lou, Environmental Cracking and Irradiation Resistant Stainless Steels by Additive Manufacturing, Idaho Falls, ID (United States), 2018. doi:10.2172/1431212.
[4] S. Anderson, G. Baca, M. O'Connor, NEET-AMM Final Technical Report on Laser Direct Manufacturing (LDM) for Nuclear Power Components, Idaho Falls, ID (United States), 2015. doi:10.2172/1233481.
[5] W.J. Sames, F.A. List, S. Pannala, R.R. Dehoff, S.S. Babu, The metallurgy and processing science of metal additive manufacturing, Int. Mater. Rev. 61 (2016) 315–360, doi:10.1080/09506608.2015.1116649.
[6] D. Herzog, V. Seyda, E. Wycisk, C. Emmelmann, Additive manufacturing of metals, Acta Mater. 117 (2016) 371–392, doi:10.1016/j.actamat.2016.07.019.
[7] M.S. Pham, B. Dovgyy, P.A. Hooper, Twinning induced plasticity in austenitic stainless steel 316L made by additive manufacturing, Mater. Sci. Eng. A 704 (2017) 102–111, doi:10.1016/j.msea.2017.07.082.
[8] M. Ziętala, T. Durejko, M. Polański, I. Kunce, T. Płociński, W. Zieliński, M. Łazińska, W. Stępniowski, T. Czujko, K.J. Kurzydłowski, Z. Bojar, The microstructure, mechanical properties and corrosion resistance of 316L stainless steel fabricated using laser engineered net shaping, Mater. Sci. Eng. A 677 (2016) 1–10, doi:10.1016/j.msea.2016.09.028.
[9] J. Hou, W. Chen, Z. Chen, K. Zhang, A. Huang, A. Juan Hou, W. Chen, Z. Chen, K. Zhang, Microstructure, tensile properties and mechanical anisotropy of selective laser melted 304L stainless steel, J. Mater. Sci. Technol (2020), doi:10.1016/j.jmst.2020.01.011.
[10] K. Saeidi, L. Kvetková, F. Lofaj, Z. Shen, Austenitic stainless steel strengthened by the in situ formation of oxide nanoinclusions, RSC Adv. 5 (2015) 20747–20750, doi:10.1039/C4RA16721J.
[11] G.S. WAS, Fundamentals of Radiation Materials Science, Springer New York, New York, NY, 2017, doi:10.1007/978-1-4939-3438-6.
[12] S.H. Li, J.T. Li, W.Z. Han, Radiation-induced helium bubbles in metals, Mater. (Basel) 12 (2019) 1–32, doi:10.3390/ma12071036.
[13] H. Trinkaus, B.N. Singh, Helium accumulation in metals during irradiation - Where do we stand? J. Nucl. Mater. 323 (2003) 229–242, doi:10.1016/j.jnucmat.2003.09.001.
[14] P.D. Edmondson, C.M. Parish, Y. Zhang, A. Hallén, M.K. Miller, Helium entrapment in a nanostructured ferritic alloy, Scr. Mater. 65 (2011) 731–734, doi:10.1016/j.scriptamat.2011.07.024.
[15] S. Nogami, A. Hasegawa, T. Tanno, K. Imasaki, K. Abe, High-temperature helium embrittlement of 316FR steel, J. Nucl. Sci. Technol. 48 (2011) 130–134, doi:10.1080/18811248.2011.9711687.
[16] P.D. Edmondson, C.M. Parish, Y. Zhang, A. Hallén, M.K. Miller, Helium bubble distributions in a nanostructured ferritic alloy, J. Nucl. Mater. 434 (2013) 210–216, doi:10.1016/j.jnucmat.2012.11.049.
[17] F.W. Wiffen, E.E. Bloom, Effect of high helium content on stainless steel swelling, Nucl. Technol. 25 (1975) 113–123, doi:10.13182/NT75-A24354.
[18] B.B. Glasgow, A. Si-Ahmed, W.G. Wolfer, F.A. Garner, Helium bubble formation and swelling in metals, J. Nucl. Mater. 104 (1981) 981–986, doi:10.1016/0022-3115(82)90727-9.
[19] L. Jia, X. He, S. Wu, D. Wang, H. Cao, Y. Dou, W. Yang, Study of helium bubble induced hardening in BCC-Fe by molecular dynamics simulation, Mater. Sci. Forum (2018) 378–386 944 MSF, doi:10.4028/www.scientific.net/MSF.944.378.
[20] S. Das, H. Yu, E. Tarleton, F. Hofmann, Hardening and strain localisation in helium-ion-implanted Tungsten, Sci. Rep. 9 (2019) 1–14, doi:10.1038/s41598-019-54753-3.
[21] G. Ackland, Controlling radiation damage, Science (80-.) 327 (2010) 1587–1588, doi:10.1126/science.1188088.
[22] X. Zhang, K. Hattar, Y. Chen, L. Shao, J. Li, C. Sun, K. Yu, N. Li, M.L. Taheri, H. Wang, J. Wang, M. Nastasi, Radiation damage in nanostructured materials, Prog. Mater. Sci. 96 (2018) 217–321, doi:10.1016/j.pmatsci.2018.03.002.
[23] S.J. Zinkle, L.L. Snead, Designing radiation resistance in materials for fusion energy, Annu. Rev. Mater. Res. 44 (2014) 241–267, doi:10.1146/annurev-matsci-070813-113627.
[24] B. Radiguet, A. Etienne, P. Pareige, X. Sauvage, R. Valiev, Irradiation behavior of nanostructured 316 austenitic stainless steel, J. Mater. Sci. 43 (2008) 7338–7343, doi:10.1007/s10853-008-2875-8.
[25] P.B.R. Rajan, I. Monnet, E. Hug, A. Etienne, N. Enikeev, C. Keller, X. Sauvage, R. Valiev, B. Radiguet, Irradiation resistance of a nanostructured 316 austenitic stainless steel, IOP Conf. Ser. Mater. Sci. Eng. (2014) 63, doi:10.1088/1757-899X/63/1/012121.

[26] E. Hug, R. Prasath Babu, I. Monnet, A. Etienne, F. Moisy, V. Pralong, N. Enikeev, M. Abramova, X. Sauvage, B. Radiguet, Impact of the nanostructuration on the corrosion resistance and hardness of irradiated 316 austenitic stainless steels, Appl. Surf. Sci. 392 (2017) 1026–1035, doi:10.1016/j.apsusc.2016.09.110.
[27] R. Schäublin, A. Ramar, N. Baluc, V. de Castro, M. Monge, T. Leguey, N. Schmid, C. Bonjour, Microstructural development under irradiation in European ODS ferritic/martensitic steels, J. Nucl. Mater. 351 (2006) 247–260, doi:10.1016/j.jnucmat.2006.02.005.
[28] M.-L. Lescoat, J. Ribis, A. Gentils, O. Kaïtasov, Y. de Carlan, A. Legris, In situ TEM study of the stability of nano-oxides in ODS steels under ion-irradiation, J. Nucl. Mater. 428 (2012) 176–182, doi:10.1016/j.jnucmat.2011.12.009.
[29] A.I. Ryazanov, O.K. Chugunov, S.M. Ivanov, S.T. Latushkin, R. Lindau, A. Möslang, A.A. Nikitina, K.E. Prikhodko, E.V. Semenov, V.N. Unezhev, P.V. Vladimirov, Tensile properties and microstructure of helium implanted EUROFER ODS, J. Nucl. Mater. 442 (2013) S153–S157, doi:10.1016/j.jnucmat.2013.03.080.
[30] Y. Zhong, L. Liu, S. Wikman, D. Cui, Z. Shen, Intragranular cellular segregation network structure strengthening 316L stainless steel prepared by selective laser melting, J. Nucl. Mater. 470 (2016) 170–178, doi:10.1016/j.jnucmat.2015.12.034.
[31] K. Saeidi, F. Akhtar, Subgrain-controlled grain growth in the laser-melted 316L promoting strength at high temperatures, R. Soc. Open Sci. 5 (2018) 172394, doi:10.1098/rsos.172394.
[32] K. Saeidi, X. Gao, Y. Zhong, Z.J. Shen, Hardened austenite steel with columnar sub-grain structure formed by laser melting, Mater. Sci. Eng. A 625 (2015) 221–229, doi:10.1016/j.msea.2014.12.018.
[33] Y.M. Wang, T. Voisin, J.T. McKeown, J. Ye, N.P. Calta, Z. Li, Z. Zeng, Y. Zhang, W. Chen, T.T. Roehling, R.T. Ott, M.K. Santala, P.J. Depond, M.J. Matthews, A.V. Hamza, T. Zhu, Additively manufactured hierarchical stainless steels with high strength and ductility, Nat. Mater. 17 (2018) 63–71, doi:10.1038/nmat5021.
[34] C. Sun, F.A. Garner, L. Shao, X. Zhang, S.A. Maloy, Influence of injected interstitials on the void swelling in two structural variants of 304L stainless steel induced by self-ion irradiation at 500°C, Nucl. Instrum. Methods Phys. Res. Sect. B Beam Interact. Mater. Atoms 409 (2017) 323–327, doi:10.1016/j.nimb.2017.03.070.
[35] I. Shibahara, S. Ukai, S. Onose, S. Shikakura, Irradiation performance of modified 316 stainless steel for Monju fuel, J. Nucl. Mater. 204 (1993) 131–140, doi:10.1016/0022-3115(93)90209-H.
[36] B. Goel, Helium production in stainless steel, Nucl. Sci. Eng. 69 (1) (1979) (United States), doi:10.13182/NSE79-A21291.
[37] P. Deng, Q. Peng, E.-H. Han, W. Ke, C. Sun, Z. Jiao, Effect of irradiation on corrosion of 304 nuclear grade stainless steel in simulated PWR primary water, Corros. Sci. 127 (2017) 91–100, doi:10.1016/j.corsci.2017.08.010.
[38] Z. Shang, C. Fan, S. Xue, J. Ding, J. Li, T. Voisin, Y.M. Wang, H. Wang, X. Zhang, Response of solidification cellular structures in additively manufactured 316 stainless steel to heavy ion irradiation: an in situ study, Mater. Res. Lett. 7 (2019) 290–297, doi:10.1080/21663831.2019.1604442.
[39] X. Sun, F. Chen, H. Huang, J. Lin, X. Tang, Effects of interfaces on the helium bubble formation and radiation hardening of an austenitic stainless steel achieved by additive manufacturing, Appl. Surf. Sci. 467–468 (2019) 1134–1139, doi:10.1016/j.apsusc.2018.10.268.
[40] M. Song, M. Wang, X. Lou, R.B. Rebak, G.S. Was, Radiation damage and irradiation-assisted stress corrosion cracking of additively manufactured 316L stainless steels, J. Nucl. Mater. 513 (2019) 33–44, doi:10.1016/j.jnucmat.2018.10.044.
[41] D. Féron, E. Herms, B. Tanguy, Behavior of stainless steels in pressurized water reactor primary circuits, J. Nucl. Mater. 427 (2012) 364–377, doi:10.1016/j.jnucmat.2012.03.034.
[42] J.F. Ziegler, M.D. Ziegler, J.P. Biersack, SRIM - The stopping and range of ions in matter (2010), Nucl. Instrum. Methods Phys. Res. Sect. B Beam Interact. Mater. Atoms. 268 (2010) 1818–1823, doi:10.1016/j.nimb.2010.02.091.
[43] X. Lou, P.L. Andresen, R.B. Rebak, Oxide inclusions in laser additive manufactured stainless steel and their effects on impact toughness and stress corrosion cracking behavior, J. Nucl. Mater. 499 (2018) 182–190, doi:10.1016/j.jnucmat.2017.11.036.
[44] B.P. Eftink, J.S. Weaver, J.A. Valdez, V. Livescu, D. Chen, Y. Wang, C. Knapp, N.A. Mara, S.A. Maloy, G.T. Gray, Proton irradiation and characterization of additively manufactured 304L stainless steels, J. Nucl. Mater. 531 (2020) 152007, doi:10.1016/j.jnucmat.2020.152007.
[45] M.A. Tschopp, K.N. Solanki, F. Gao, X. Sun, M.A. Khaleel, M.F. Horstemeyer, Probing grain boundary sink strength at the nanoscale: Energetics and length scales of vacancy and interstitial absorption by grain boundaries in α-Fe, Phys. Rev. B - Condens. Matter Mater. Phys. 85 (2012) 1–21, doi:10.1103/PhysRevB.85.064108.
[46] R. Bullough, M.R. Hayns, M.H. Wood, Sink strengths for thin film surfaces and grain boundaries, J. Nucl. Mater. 90 (1980) 44–59, doi:10.1016/0022-3115(80)90244-5.
[47] A.A. Kohnert, L. Capolungo, Sink strength and dislocation bias of three-dimensional microstructures, Phys. Rev. Mater. 3 (2019) 1–12, doi:10.1103/PhysRevMaterials.3.053608.
[48] L.K. Mansur, Theory and experimental background on dimensional changes in irradiated alloys, J. Nucl. Mater. 216 (1994) 97–123, doi:10.1016/0022-3115(94)90009-4.
[49] N. Li, Y.D. Wang, W.J. Liu, Z.N. An, J.P. Liu, R. Su, J. Li, P.K. Liaw, In situ X-ray microdiffraction study of deformation-induced phase transformation in 304 austenitic stainless steel, Acta Mater. 64 (2014) 12–23, doi:10.1016/j.actamat.2013.11.001.
[50] T. Shintani, Y. Murata, Evaluation of the dislocation density and dislocation character in cold rolled Type 304 steel determined by profile analysis of X-ray diffraction, Acta Mater. 59 (2011) 4314–4322, doi:10.1016/j.actamat.2011.03.055.
[51] C. Sun, S. Zheng, C.C. Wei, Y. Wu, L. Shao, Y. Yang, K.T. Hartwig, S.A. Maloy, S.J. Zinkle, T.R. Allen, H. Wang, X. Zhang, Superior radiation-resistant nanoengineered austenitic 304L stainless steel for applications in extreme radiation environments, Sci. Rep. 5 (2015) 1–7, doi:10.1038/srep07801.
[52] X. Zhang, K. Hattar, Y. Chen, L. Shao, J. Li, C. Sun, K. Yu, N. Li, M.L. Taheri, H. Wang, J. Wang, M. Nastasi, Radiation damage in nanostructured materials, Prog. Mater. Sci. 96 (2018) 217–321, doi:10.1016/J.PMATSCI.2018.03.002.
[53] F.A. Garner, Radiation damage in austenitic steels, in: Comprehensive Nuclear Materials, 1st ed., Elsevier Inc, 2012, pp. 33–95, doi:10.1016/B978-0-08-056033-5.00065-3.